Journal of
Synchrotron
Radiation

ISSN 0909-0495

Received 26 December 2007
Accepted 10 March 2008

In situ observation of water distribution and behaviour in a polymer electrolyte fuel cell by synchrotron X-ray imaging

Taihei Mukaide,[a]* Satoshi Mogi,[b] Jun Yamamoto,[b] Akira Morita,[b] Shinnosuke Koji,[b] Kazuhiro Takada,[a] Kentaro Uesugi,[c] Kentaro Kajiwara[c] and Takashi Noma[a]

[a]Canon Research Center, Canon INC, Japan, [b]SFC Technology Project, Canon INC, Japan, and [c]Japan Synchrotron Radiation Research Institute, Japan. E-mail: mukaide.taihei@canon.co.jp

In situ visualization of the distribution and behaviour of water in a polymer electrolyte fuel cell during power generation has been demonstrated using a synchrotron X-ray imaging technique. Images were recorded using a CCD detector combined with a scintillator (Gd_2O_2S:Tb) and relay lens system, which were placed at 2.0 m or 2.5 m from the fuel cell. The images were measured continuously before and during power generation, and data on cell performance was recorded. The change of water distribution during power generation was obtained from X-ray images normalized with the initial state of the fuel cell. Compared with other techniques for visualizing the water in fuel cells, this technique enables the water distribution and behaviour in the fuel cell to be visualized during power generation with high spatial resolution. In particular, the effects of the specifications of the gas diffusion layer on the cathode side of the fuel cell on the distribution of water were efficiently identified. This is a very powerful technique for investigating the mechanism of water flow within the fuel cell and the relationship between water behaviour and cell performance.

Keywords: *in situ* synchrotron X-ray imaging; polymer electrolyte fuel cell.

1. Introduction

Fuel cells are attractive as next-generation power sources because they generate power efficiently and produce no pollutants such as nitrogen oxide. Fuel cells can be categorized into solid-oxide fuel cells (SOFC), molten carbonate fuel cells (MCFC), phosphoric acid fuel cells (PAFC), polymer electrolyte fuel cells (PEFC) and so on (Steele & Heinzel, 2001; Perry & Fuller, 2002). Among these types, the PEFC is suitable for automobiles, home use and as a mobile power generator since it can run at a lower temperature than the other types.

A schematic diagram of power generation by a PEFC is shown in Fig. 1. Hydrogen is fed from the anode side of the PEFC and is decomposed to protons and electrons at the surface of the anode electrochemical catalyst. The anodic reaction is given by

$$H_2 \rightarrow 2H^+ + 2e^-. \quad (1)$$

The electrons are supplied to the cathode through an interconnection and the protons are supplied to the cathode through a proton-exchange membrane. Then, water is synthesized by oxygen reduction reaction (ORR) of the protons, electrons and oxygen at the point of the triple-phase interface, which is composed of cathode electrochemical catalyst, proton-exchange electrolyte membrane and oxygen. The ORR is given by

$$1/2O_2 + 2H^+ + 2e^- \rightarrow H_2O. \quad (2)$$

One of the most important factors for stable power generation by the PEFC is appropriate management of the water in the PEFC. Generally, perfluorosulfonate polymers such as Nafion are used as the proton-exchange membrane of a PEFC. Excessive release of water from the PEFC causes the proton-exchange membrane to dry out and destabilizes power generation because water in the membrane is necessary to transport the protons. This phenomenon is called 'dry out'. On the other hand, too much liquid water remaining in the PEFC also inhibits power generation since the liquid water covers the triple-phase interface or the path of gas and blocks the transport of oxygen. This phenomenon is called 'flooding'. Therefore, we need to control the quantity of water in the PEFC appropriately according to the power operation conditions.

To do this, we need to know the relationships between the distribution and behaviour of the water, and the operating conditions and constituent elements of the PEFC. Based on theoretical studies of PEFCs, numerous mathematical models of the behaviour of water in the PEFC have been proposed (*e.g.* Springer *et al.*, 1991; Um & Wang, 2006). Furthermore,

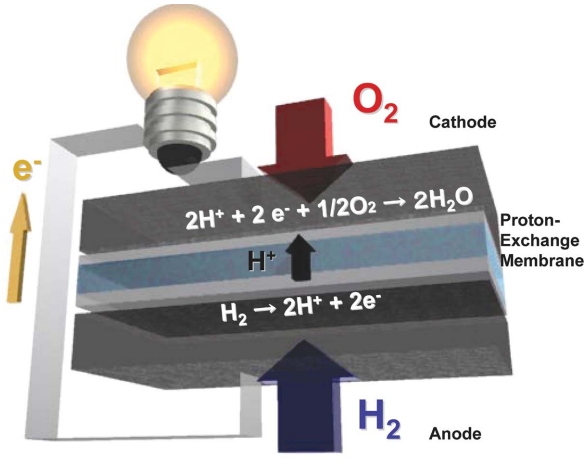

Figure 1
Schematic diagram of the power generation processes in a PEFC. The PEFC generates electricity by oxygen reduction reaction at the cathode triple-phase interface, which is composed of catalyst, proton-exchange electrolyte membrane and oxygen.

some *in situ* measurement techniques for visualizing the water behaviour have been demonstrated recently. One of these is an optical microscope technique (Zhang & Wang, 2006; Tüber *et al.*, 2003). This technique can measure the removal of water droplets from the gas diffusion layer (GDL) of the PEFC (Zhang & Wang, 2006) and is superior in terms of spatial and temporal resolution, but it cannot detect the water distribution within the PEFC. Furthermore, with this technique it is difficult to quantify the water content. The use of magnetic resonance imaging to measure the distribution of water in a proton-exchange membrane was also demonstrated (Teranishi *et al.*, 2005), but the technique has a problem that the components of the fuel cell must be made of non-magnetic materials.

One of the most powerful techniques is neutron radiography (Geiger *et al.*, 2002; Hickner *et al.*, 2006). Neutrons offer excellent penetration of the materials comprising the fuel cell and are sensitive to light element compounds such as water, but a disadvantage of this technique is low spatial resolution (>150 µm). Higher spatial resolution is very important for observing the distribution and behaviour of liquid water in the fine structures that affect the water-retaining function of the PEFC.

X-ray radiography is another powerful non-destructive imaging technique, but, comparing neutron radiography measurement for light element materials, the cross section for these materials is not sufficient in the case of hard X-rays. Furthermore, it is necessary to use higher-energy X-rays in this case because the water is synthesized within the fuel cell, the components of which are made of higher-density materials than water. One solution towards this problem is to detect the phase-shift effect of X-rays by objects (Snigirev *et al.*, 1995; Wilkins *et al.*, 1996; Suzuki *et al.*, 2002; Sera *et al.*, 2005). The complex refractive index for X-rays is given by

$$n = 1 - \delta - i\beta, \qquad (3)$$

where δ is the refractive index decrement for the phase shift and β is responsible for X-ray absorption. Because δ is about three orders of magnitude larger than β in the case of water in the hard X-ray region, visibility for water is improved by detecting the effect of diffraction or refraction of X-rays. One of the most simple and useful techniques of X-ray phase imaging is to record an image at a distance far from the sample, which is called refraction-enhanced imaging or propagation-based phase imaging. Such a recorded image contains edge-enhanced effects by objects. As a result, the visibility of water droplets in a PEFC is expected to be improved by using this method. Furthermore, it is considered that high brilliance and coherent synchrotron X-rays permit real-time observation of refraction-enhanced images of water in the fuel cell.

In this study, we used the synchrotron X-ray imaging technique to observe the distribution and behaviour of liquid water created by ORR in the PEFC.

2. Experimental

Experiments were performed at BL19B2 and BL20B2 of SPring-8. Details of BL20B2 have been reported previously (Goto *et al.*, 2001). A schematic illustration of the experimental set-up is shown in Fig. 2. Experimental hutches were placed at 111 m (BL19B2) and 206 m (BL20B2) from the light source. White X-rays from the light source were monochromated at 30 keV by the Si (111) double-crystal monochromator. The X-ray beam was shaped like a rectangle, the size of which was the same as the field of view of the X-ray image detector by the slits. An ionization chamber was used to monitor fluctuations of incident X-rays. The PEFC was placed on the sample stage, which was composed of *XYZ* stages, swivel stages (*Rx*, *Ry*) which rotated around the *X* or *Y* axis, and a rotation stage (ω) which rotated around the *Z* axis. The X-rays transmitted from the PEFC were detected by an X-ray image detector which was composed of a CCD detector [C4880-50-24A (1024 pixels × 1024 pixels) or C4742-95-12HR

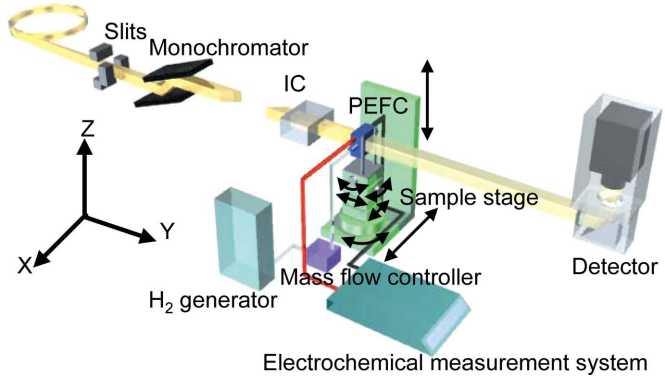

Figure 2
Schematic illustration of the experimental set-up of this study. A monochromatic rectangle X-ray beam was irradiated on the PEFC and the transmitted X-ray beam was recorded using a two-dimensional X-ray detector as an image. Images were measured continuously before and during power generation.

(4000 pixels × 2624 pixels), Hamamatsu Photonics], a scintillator (Gd_2O_2S:Tb) and relay lens system (Suzuki *et al.*, 1999). The effective pixel size of each detector was 6.3 µm × 6.3 µm and 5.9 µm × 5.9 µm and the spatial resolution was about 12 µm. The distance between the PEFC and the detector was between 2.0 m and 2.5 m for obtaining edge-enhanced images when the size of water droplets was much greater than the spatial resolution of the detector. A schematic illustration of a typical PEFC as used in this study is shown in Fig. 3.

The PEFC was composed of several layers. In this study, Nafion112 was used as the proton-exchange membrane. This proton-exchange membrane was sandwiched by catalyst layers. The catalyst was platinum nanopowder or a porous Pt film with thicknesses of 10 µm and 2 µm, respectively. The area of the catalyst layer was 20 mm × 7.5 mm. Generally, a collection of these three types of layer is called a membrane electrode assembly (MEA). Furthermore, carbon cloth or carbon paper with a microporous layer (E-TEK) as a GDL was placed on the outer side of each catalyst layer. On the cathode side, a metal foam (Mitsubishi Materials) made of stainless steel was used as the gas flow channel and was placed on the MEA. The porosity of the metal foam was more than 90% and the pore diameter was about 600 µm. Then, these layers were sandwiched by aluminium or stainless steel plates as current collectors. The PEFC was placed in two directions on the sample stage: either the layers were parallel to the incident X-rays for observing the distribution of water in the depth direction of each layer, or the layers were perpendicular to the incident X-rays for observing the in-plane distribution of water of the layers. Power generation was performed by supplying air to the cathode side and hydrogen gas to the anode side. Hydrogen gas was generated by the electrolysis reaction of water by a hydrogen generator (OPGU-2100, STEC) and air was self-breathing through the metal foam.

Measurement of images was performed continuously during measurement of the polarization curve at room temperature and experimental hutch humidity conditions (about 27%) in this study. The exposure time of each image was between 1 s and 4 s under the condition of the components of the PEFC.

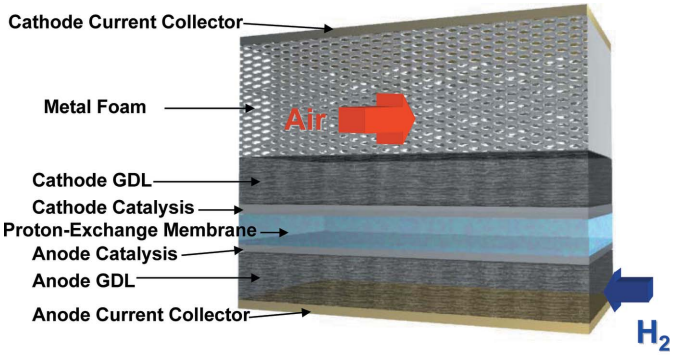

Figure 3
Schematic illustration within the PEFC. The PEFC was composed of several layers: the cathode and anode current collectors, metal foam, cathode and anode gas diffusion layers, cathode and anode catalyst layers and a proton-exchange membrane. Hydrogen gas was supplied on the right-hand side of the anode gas diffusion layer and air gas was supplied by self-breathing through the metal foam.

3. Results and discussion

Fig. 4 shows an example of *in situ* images measured at BL19B2. The GDL of the PEFC was carbon cloth and the catalyst was porous Pt film. In this case, these layers were perpendicular to the incident X-rays. Fig. 4(*a*) shows a photograph of the PEFC. The white rectangle indicates the outline of the measurement area. The CCD camera in this measurement was a C4880-50-24A. Fig. 4(*b*) shows a raw image before power generation. Because the texture of the metal foam occupies most of the image, it was difficult to recognize the water distribution and behaviour from the raw image only during power generation. The intensity of X-rays transmitted from the sample during power generation is given by Beer–Lambert's law,

$$I = I_0 A \exp(-\mu \Delta l), \tag{4}$$

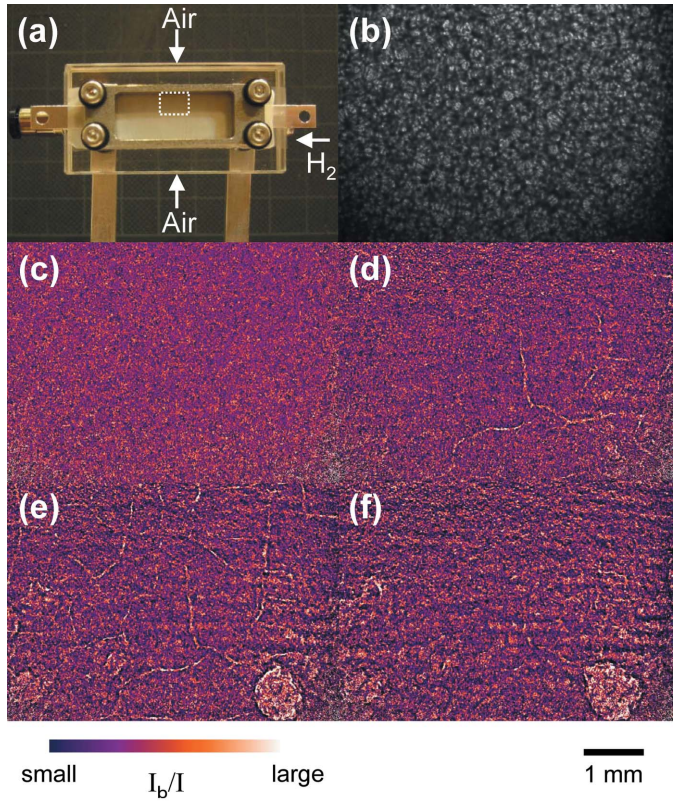

Figure 4
Some images for measuring the distribution and behaviour of water in the PEFC in which the MEA was composed of Nafion112 and porous Pt film, and the GDL was carbon cloth. (*a*) Photograph of the PEFC. The white square is the observed area. (*b*) Raw image of the PEFC before power generation. (*c*)–(*e*) Analysed images during measurement of the polarization curve, at a current sweep rate of 0.1 mA cm^{-2} s. The current densities were 7 mA cm^{-2} (*c*), 105 mA cm^{-2} (*d*) and 190 mA cm^{-2} (*e*). (*f*) An analysed image after flooding. This measurement was performed at BL19B2. The scale bar for (*c*)–(*e*) is 1 mm. The look-up table is represented by I_b/I, where I_b and I correspond to the X-ray intensity before and during power generation.

where I_0 is the intensity of the incident X-ray beam, A is responsible for X-ray absorption by elements comprising the PEFC and is a constant obtained from the intensity of X-rays transmitted before power generation, μ is the linear absorption coefficient of water, and Δl is the length of water in the X-ray transmission direction. Therefore, an image of only liquid water distribution can be obtained by analysing images recorded before and during power generation. Figs. 4(*c*)–(*f*) show images of the water distribution during power generation. These images were obtained by dividing the images recorded during power generation into an image recorded before power generation after subtracting the dark-current image and normalizing by the intensity of incident X-rays.

The polarization curve for this measurement is shown in Fig. 5. The value of the potential suddenly decreased at about 220 mA cm^{-2} owing to flooding. The behaviour of the water in this PEFC during measurement of the polarization curve was categorized into several parts. In the region up to 40 mA cm^{-2}, generated water was mainly absorbed by the proton-exchange membrane or exited from the PEFC as water vapour (Fig. 4*c*). Though the theoretical potential is about 1.23 V, the real cell potential was lower. Under such low-current-density conditions, the loss mechanism is mainly activation overpotential, the main cause of which is sluggish ORR at the cathode catalyst layer. The shape of the polarization curve caused by the activation overpotential is given by Tafel's equation,

$$\eta = a + b\log(i), \tag{5}$$

where η is the overpotential, i is the current density, and a and b are constants. The Tafel slope calculated from the polarization curve was -115 mV per decade.

Next, liquid water filled cracks in the PEFC at 90 mA cm^{-2}, the width of which was about 50 µm, and spread as current density was heightening (Fig. 4*d*). The shape of the polarization curve in this region was caused mainly by ohmic losses. The potential at current densities from 40 mA cm^{-2} to 70 mA cm^{-2} increased slightly because the resistance of the proton-exchange membrane decreased with absorption of water. In the region of higher current density, water droplets appeared in the PEFC (Fig. 4*e*). Around this current density condition, the mass diffusion overpotential strongly affected the shape of the polarization curve. This was partly due to mass transport limitation caused by water filling the path of the oxygen gas. Finally, the water droplets remained but liquid water in the cracks disappeared after the flooding condition (Fig. 4*f*). From these observations, the cracks could be seen closer to the catalyst layer than the water droplets. The disappearance of liquid water in the cracks was considered to be caused by inverse diffusion for the MEA.

Fig. 6 shows an image of the same type of PEFC measured when X-rays entered parallel to the MEA. There were some channels of width ~50 µm at the MEA/GDL interface. This means that these channels were inhabited at the microporous layer of the GDL. Then, the water shown in Fig. 4(*d*) moved along the channel from the catalyst layer. On the other hand, the water droplets shown in Fig. 4(*e*) were considered to be shaped in the metal foam.

From the results of this measurement, we demonstrate the observation of water distribution and behaviour in two types of PEFC. In one type, normal carbon paper was used as the cathode GDL. The cathode GDL of the other type had a pinhole array that ran transverse across the GDL. The diameter of the pinholes was 110 µm. A Pt nanopowder was used as the catalyst for both types of PEFC. These experiments were performed at BL20B2. The current density sweep rate was 0.4 mA cm^{-2} s. Figs. 7(*a*)–7(*d*) show images of a PEFC in which the cathode GDL had no pinholes. Fig. 7(*a*) shows the raw image of the PEFC before power generation and Figs. 7(*b*)–7(*d*) show the analysed image during power generation. The values of current density of these images were 120 mA cm^{-2} (*b*), 242 mA cm^{-2} (*c*) and 346 mA cm^{-2} (*d*). There were inhomogeneous distributions of water in the GDL. The most serious cause of inhomogeneity of water distribution in this GDL was considered to be an inhomogeneous distribution of pores in the GDL. Under the high current density condition (Fig. 7*d*), water condensation appeared at the metal-foam/current-collector interface. The reason for the water condensation was the temperature gradient in the PEFC; the

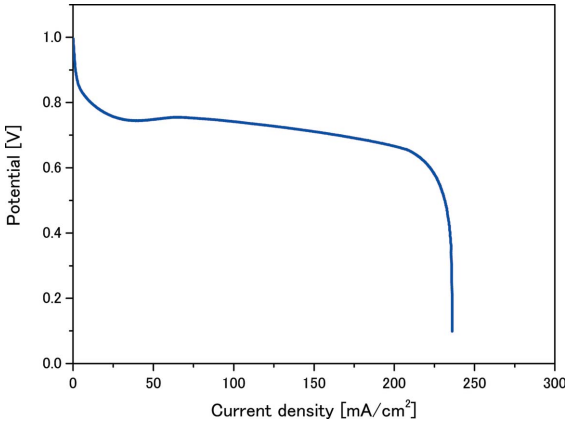

Figure 5
Polarization curve of the PEFC of Fig. 4. The current density sweep rate was 0.1 mA cm^{-2} s. The flooding started at ~220 mA cm^{-2}.

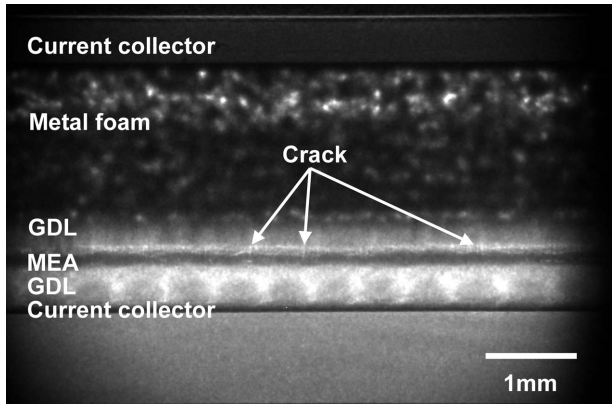

Figure 6
Cross-section image of the PEFC in which the MEA was composed of Nafion112 and porous Pt film, and the GDL was carbon cloth. There were some vertical line textures around the MEA/cathode GDL interface.

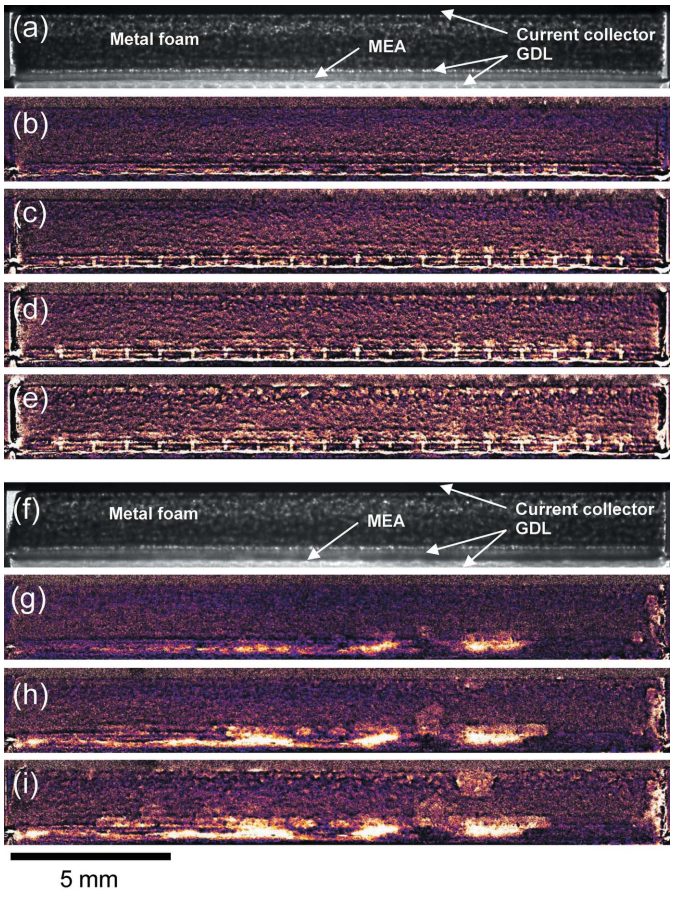

Figure 7
Cross-section images of water distribution of two PEFCs. One contained a normal GDL with carbon paper (*a*)–(*d*), and the other contained a modified GDL at the cathode side (*e*)–(*i*). The modified GDL contained carbon paper and had a pinhole array perpendicular to the GDL. (*a*),(*e*) Raw images of these PEFCs before power generation. (*b*)–(*d*), (*f*)–(*i*) Water distribution images of each PEFC during power generation. Current densities were 120 mA cm^{-2} (*b*), 242 mA cm^{-2} (*c*), 346 mA cm^{-2} (*d*), 91 mA cm^{-2} (*f*), 152 mA cm^{-2} (*g*), 242 mA cm^{-2} (*h*) and 373 mA cm^{-2} (*i*). Pt nanopowder was used as the catalyst of these PEFCs. The sweep rate of current density was 0.4 mA cm^{-2} s. The scale bar is 5 mm.

current collector was cooler than the cathode catalyst layer which was heated by ORR.

On the other hand, Figs. 7(*e*)–7(*i*) show the results of the pinhole array GDL case. Fig. 7(*e*) shows the raw image of the PEFC before power generation and Figs. 7(*f*)–7(*i*) show the analysed image during power generation. The inlet of hydrogen gas in the anode side was on the right-hand side of these images. The current density values of these images were 91 mA cm^{-2} (*f*), 152 mA cm^{-2} (*g*), 242 mA cm^{-2} (*h*) and 373 mA cm^{-2} (*i*). The liquid water flowed into the pinholes from the inlet side of the hydrogen gas to the opposite side selectively as shown in Figs. 7(*f*)–7(*g*). This indicates inhomogeneity of the power generation at the catalyst layer of the cathode side which is related to the position from the hydrogen gas inlet. In order to interpret these selective flows in the cracks shown in Fig. 4 or pinholes of the cathode GDL, an idealized model of the GDL was assumed. This GDL has only cylindrical pores that run transverse across the GDL. In this case, if water enters the pores, the pressure gradient between the metal foam and the GDL/catalyst layer interface must overcome the surface energy of the pores. The pressure difference for forcing water into the pores is given by the Young–Laplace equation,

$$\Delta P = \frac{2E_{\text{water}} \cos\theta}{r}, \tag{6}$$

where E_{water} is the surface energy of water, θ is the contact angle of water for the surface of the pore and r is the radius of the pore. The carbon paper and carbon cloth are hydrophobic. As the radius of pores increases, the pressure difference decreases. In this study, the radius of the cylindrical pores of the pinhole GDL was larger than that of other pores in the GDL. As a result, the water created by ORR at the triple-phase interface flowed into the pinhole pores selectively. Furthermore, this result indicated the possibility of achieving more selective water flow in the GDL by controlling the hydrophobic/hydrophilic properties of the GDL or radius of the pores.

As the current density increased, the water in the metal foam super-added from the outlet of each pinhole as shown in Figs. 7(*h*)–7(*i*). Furthermore, water condensation appeared at the metal-foam/current-collector interface.

4. Conclusion

A synchrotron X-ray imaging technique was used to observe the water distribution and behaviour in PEFCs during power generation. Using this technique, the water distribution and behaviour were clarified with high spatial resolution in the components of the PEFC such as GDL or foam metal at the same time.

This technique is very powerful for verifying the mechanism of water flow in PEFC under several conditions such as component materials of the PEFC or power generation. The technique is also useful for comparing numerous models of water distribution with actual distributions with high spatial resolution.

We have been improving the X-ray imaging system such as controlling the humidity of the air and temperature conditions of PEFC. We have also improved the spatial resolution of the detector to observe the distribution in the proton-exchange membrane. Details of these studies will be reported in the future.

The synchrotron radiation experiments were performed at BL19B2 and BL20B2 of SPring-8 with the approval of the Japan Synchrotron Radiation Research Institute (JASRI) (proposal numbers 2004B0991-RI-np, 2005A0271-NI-p and 2006B0167).

References

Geiger, A. B., Tsukada, A., Lehomann, E., Vontobel, P., Wokaun, A. & Scherer, G. G. (2002). *Fuel Cells*, **2**, 92–98.
Goto, S., Takeshita, K., Suzuki, Y., Ohashi, H., Asano, Y., Kimura, H., Matsushita, T., Yagi, N., Isshiki, M., Yamazaki, H., Yoneda, Y.,

Umetani, K. & Ishikawa, T. (2001). *Nucl. Instrum Methods*, A**467–468**, 682–685.
Hickner, M. A., Siegel, N. P., Chen, K. S., McBrayer, D. N., Hussey, D. S., Jacobson, D. L. & Arif, M. (2006). *J. Electrochem. Soc.* **153**, A902–A908.
Perry, M. L. & Fuller, T. F. (2002). *J. Electrochem. Soc.* **149**, S59–S67.
Sera, T., Uesugi, K. & Yagi, N. (2005). *Med. Phys.* **32**, 2787–2792.
Snigirev, A., Snigireva, I., Kohn, V., Kuznetsov, S. & Schelokov, I. (1995). *Rev. Sci. Instrum.* **66**, 5486–5492.
Springer, T. E., Zawodzinski, T. A. & Gottesfeld, S. (1991). *J. Electrochem. Soc.* **138**, 2334–2342.
Steele, B. C. H. & Heinzel, A. (2001). *Nature (London)*, **414**, 345–352.
Suzuki, Y., Yagi, N. & Uesugi, K. (2002). *J. Synchrotron Rad.* **9**, 160–165.
Suzuki, Y., Yagi, N., Umetani, K., Kohmura, Y. & Yamasaki, K. (1999). *Proc. SPIE*, **3770**, 13–22.
Teranishi, K., Tsushima, S. & Hirai, S. (2005). *Electrochem. Solid-State Lett.* **8**, A281–A284.
Tüber, K., Pocza, D. & Hebling, C. (2003). *J. Power Sources*, **124**, 403–414.
Um, S. & Wang, C. (2006). *J. Power Sources*, **156**, 211–223.
Wilkins, S. W., Gureyev, T. E., Gao, D., Pogany, A. & Stevenson, A. W. (1996). *Nature (London)*, **384**, 335–338.
Zhang, F. Y. & Wang, C. Y. (2006). *J. Electrochem. Soc.* **153**, A225–A232.